Effects of process parameters and scan strategy on the microstructure and density of stainless steel 316 L produced via laser powder bed fusion

Angelos Evangelou [a,*], Rafael Stylianou [a], Alexandros Loizou [a], Donghyuk Kim [b], Anqi Liang [b], Philippa Reed [b], Georgios Constantinides [c], Theodora Kyratsi [a]

[a] Department of Mechanical and Manufacturing Engineering, University of Cyprus, Panepistimiou 1, 2109 Nicosia, Cyprus
[b] Engineering Materials Research Group, Faculty of Engineering and Physical Sciences, University of Southampton, University Road, Southampton S017 1BJ, United Kingdom
[c] Department of Mechanical Engineering and Materials Science and Engineering, Cyprus University of Technology, Archiepiskopou Kyprianou 30, 3036 Limassol, Cyprus

ABSTRACT

The ability to produce reliable and reproducible components from 316 L using additive manufacturing is crucial to serve the need for customization, on-demand manufacturing and reduced lead times for various industries. Laser powder bed fusion is becoming widely accepted as a versatile additive manufacturing technique capable of producing near defect-free components with tailored microstructures and mechanical properties. However, despite the recent progress in process parameter selection and optimization, even a small change in any of the laser parameters, equipment and feedstock powder characteristics can influence the microstructure and subsequently the mechanical properties of the fabricated parts. The purpose of this work is to tackle the process optimization challenge through, a full factorial design of experiments approach, to systematically assess the widely adopted energy density factor to evaluate the density of the final component. A statistical approach was also followed to evaluate potential plastic anisotropy in different samples produced with various energy densities and scan strategies. Density measurements indicated that beyond laser power and scan speed, the interaction effects of the aforementioned parameters with the layer thickness and the powder size distribution have a significant effect on the sample. Microstructural features such as melt pools, grains and crystallographic texture were characterized against a range of volumetric energy densities and scan strategies represented by different angles of rotation between successive layers. Smaller angles of rotation per layer were found to decrease texture anisotropy and suppress the formation of keyhole porosity in finer and more homogenous microstructures. The assessment of plastic anisotropy in the produced samples was evaluated using microhardness measurements on all three orthogonal planes of the samples. The hierarchical microstructure of laser powder bed fusion materials induces several strengthening mechanisms, that can simultaneously be activated depending on the loading scenario, location and plane.

1. Introduction

Additive manufacturing (AM) technologies are nowadays becoming a standard production method for many high-value applications that are in constant search for higher performing structures. Through the design and material freedom offered by AM, several applications have unlocked possibilities in higher strength-to-weight ratio components, reduced lead times and simplified assemblies [1]. Increasing demands driven by the potential of reaching even higher levels of optimization in terms of structural integrity, multifunctionality and weight savings, resulted in

further, ongoing developments of AM, with laser powder bed fusion (LPBF) technologies, being at the forefront of advancements [2].

These trends are reflected in the numerous, process optimization studies that include a variety of material systems aiming towards higher and more reproducible properties [3–6]. Nevertheless, despite the ongoing efforts, there is still a lack of holistic approaches or understanding that captures all aspects and phenomena that control the quality of the final AM build [7]. Processability and quality depend on several aspects including feedstock powder morphological aspects that are characteristic of the particle size distribution [8]. Other intrinsic

material considerations that affect processability include thermophysical properties such as thermal conductivity and also extend to the process-critical melting and evaporation temperatures of the feedstock powder. The flexibility offered by LPBF in terms of the ability to process a range of materials is therefore accompanied by a certain degree of complexity. Following an extensive investigation of the available literature, Yadroitsev highlighted that the quality of the final LPBF component is affected by more than 130 parameters [9]. The current consensus in the literature, however, is that the most important parameters are the laser power, scan speed, hatch spacing and powder layer thickness. These are often combined in an equation to describe the volumetric energy density (VED) that is supplied to the powder bed by the laser source.

Indeed, process parameter optimization has been the main focus of several investigations which assessed the quality of the final print against the theoretical material density and the mechanical performance of representative samples [10–13]. Different approaches have been employed in the literature to tackle optimization, with the most popular one relying on trial-and-error experimentation.

Austenitic stainless steel 316 L has been one the most widely used materials in LPBF, as it not only meets the material processing criteria in terms of processability (favourable thermophysical properties), but it can also serve a wide range of applications in the marine, aerospace, energy and biomedical industries. Functional prototypes of 316 L were produced by Zhang et al., following an investigation of single-track beads produced using different combinations of laser power, scan speed and layer thickness [13]. Inadequate VEDs characterized by low laser power and high scan speeds, lead to a balling phenomenon and a weak interfacial bonding between the track beads and the substrate. Optimal melt pools were obtained using a laser power of 100 W and a scan speed of 300 mm/s. Similar observations were made by Liu et al. [12], who found that "lower scan speeds" of 800–900 mm/s produce samples with relative densities of at least 99%. Although similar trends were observed, the lower scan speeds mentioned in the latter are three times higher than the previous study, highlighting the importance of considering the interactive effects of all the major process parameters. It is well established that VEDs below a critical threshold (resulting from any combination of the four major process parameters), lead to insufficient melting of the material which typically results in the formation of lack-of-fusion porosity. On the other hand, excessive VED can evaporate the molten metal creating keyholes [14]. Therefore, for each material, it can be argued that there is a range of processing parameters that can be combined into an optimal VED window where parts can be produced with high densities. For 316 L, Choong et al. [15], have shown that such a window exists at a VED of 100–110 J/mm^3, while Yakout et al. [16], have found that the highest densities are achieved between 62 and 104 J/mm^3.

Ultimately though, altering the LPBF process parameters and the energy imposed on the material alters the melting and solidification of the material which in turns control the growth of grains and the formation of microstructure [17]. Microstructural features of LPBF materials are formed under high temperature gradients with rapid solidification rates. These conditions result in highly complex and hierarchical microstructures that commonly include elongated grains of

different scales, overlapping melt pools and segregated elements at the melt pool boundaries as well as cellular colonies [18,19]. Consequently, material properties are often highly anisotropic and damage is controlled by several mechanisms across a range of scales [20].

The current literature indicates that the production of quality parts via LPBF is heavily dependent on process optimization which in turn controls the microstructure and final properties. Even though numerous studies have taken place, there are still significant discrepancies in the approach and range of optimal parameters for 316 L, which deem further investigations necessary. Table 1 summarizes recent parameter optimization studies for the 316 L stainless steel. Although single-track deposition studies offer a time efficient method for investigating the effect of process parameters, they do not fully reflect the physical phenomena that take place during cooling in multilayer and multi-track builds [14]. Furthermore, the majority of the available studies rely on a "one factor at a time" approach where one or two parameters are investigated at a time while the rest remain constant. This approach, however, fails to provide information regarding the interaction of parameters and often yields inconclusive results. A more comprehensive assessment of the VED effects on the density of 316 L has been reported by Yakout et al., that employed a full factorial design of experiments (DOE) study that included three levels of laser power, scan speed and hatch spacing [16]. Over the examined parameter range, they established an optimal LPBF process window, where peak density with stable consolidation of SS-316 L was achieved.

Within this work, the effect of process parameters and the effectiveness of VED as a density metric for LPBF consolidated stainless steel 316 L parts were assessed. Instead of a one-factor-at-a-time approach, this work employs a full factorial DOE approach where the effects of laser power, scan speed, hatch spacing and layer thickness are examined simultaneously. Investigations concerning the effects of scanning strategy variation were also undertaken with a particular focus on densification, microstructure and hardness response.

2. Experimental procedure

2.1. Material and LPBF processing

Feedstock material corresponding to stainless steel 316 L was supplied by Carpenter Additive (CT PowderRange 316 L E) in the form of gas atomized powder. The 316 L powder has a spherical morphology with a few satellite particles and a particle size distribution as shown in Fig. 1. An Orlas Creator RA LPBF system, equipped with a Ytterbium fibre laser emitting at 1070 nm, was used to produce cubic samples in batches of nine with dimensions of 10 × 10 × 10 mm^3. All printing occurred under a nitrogen environment (<0.5% volume fraction of O$_2$) to limit the effects of oxidation.

2.2. Design of experiments (DOE) study

This study employed a three-level full factorial analysis to investigate the effects of (a) laser power, (b) scanning speed, (c) hatch spacing, and (d) layer thickness on the resulting density and microhardness. For all samples in the parametric study, a unidirectional laser scanning pattern

Table 1
Summary of recent LPBF parameter optimization studies of 316 L.

| Power (W)	Speed (mm/s)	Hatch (μm)	Layer (μm)	Energy Density (J/mm^3)	Scan Strategy	Powder (μm)	Ref
100–150	700	50–70	20	102–204	3 × 3 mm chessboard with 30° rotation between layers	15–45	[21]
100	111–239	111–120	50	70–150	Unidirectional hatching with and without double pass and 90° rotation between layers. Also, cross hatching and no rotation between layers was investigated	30–55	[22]
185–245	800–1000	100	30	84–111	Striped tracks with 115° rotation between layers	16–33	[12]
150–200	446–1667	80–140	30	50–80	Reported as: *scanned layers deposited parallel to the horizontal plane*	-	[23]
380	625–3000	25–120	50	99–109	Bidirectional strip pattern with 45° rotation between layers	20–63	[3]
200–300	600–1000	80–120	40	42–156	Unidirectional strip pattern with 67° rotation between layers	17–49	[16]
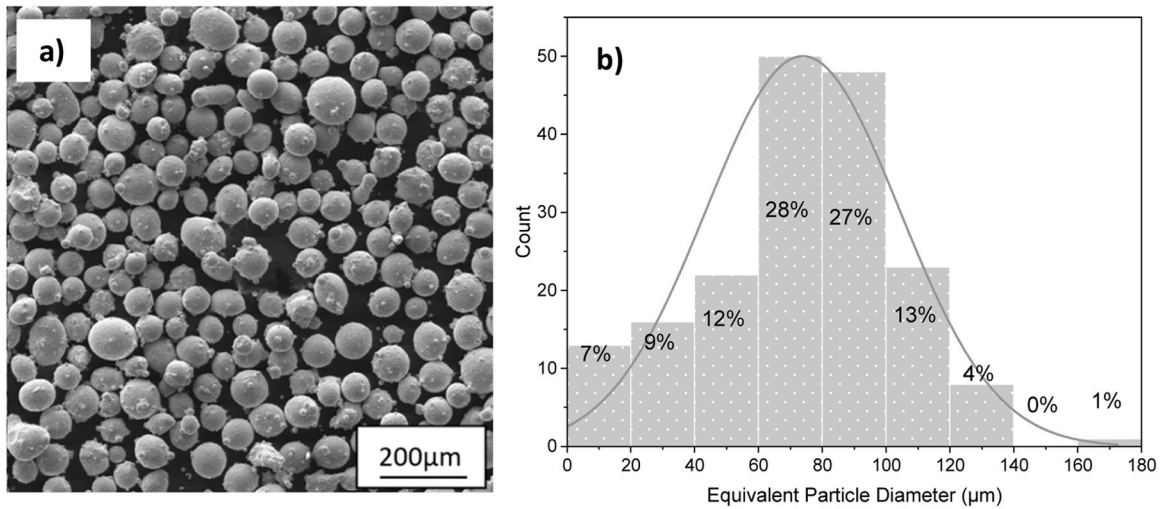
Fig. 1. (a) Morphology and (b) particle size distribution of the 316 L feedstock powder.

with no rotation between layers (Fig. 2a) was used. The DOE included 3^4 (i.e. 81) combinations of LPBF process parameters as depicted in Table 1. These parameters were combined to calculate the volumetric energy density (VED - J/mm³) which was used as a metric for quantifying the energy transferred from the LPBF machine to the 316 L powder bed. Despite its limitations in fully capturing material related effects and the complex phenomena at the melt pool, VED is a widely accepted metric for optimization studies and it is defined as follows.

$$E_d = \frac{P}{v \bullet h \bullet l} \qquad (1)$$

There, E_d corresponds to the volumetric energy density, while *P, v, h, and l* correspond to laser power, scan speed, hatch spacing, and layer thickness, respectively.

The regression model used to examine the effect of parameters was developed using Minitab and included the main effects of *P, v, h* and *l* as well as the two- and three-way interactions. Confidence intervals of 95% were used (p value > 0.05). The overall model significance was examined using an F-test, which evaluates whether the combined effects of the predictors (process parameters and combinations of process parameters) on the dependent variable (relative density) are statistically significant or due to random chance, aiding in the determination of the model's reliability and appropriateness for drawing meaningful conclusions.

2.3. Scanning strategy Investigation

Subsequent investigations included variations of the scanning strategy through the introduction of 90° and 45° shift angles between layers but with the same unidirectional scanning pattern (Fig. 2b and c). The scanning strategy investigation was implemented for representative samples from the investigated energy density range. This corresponded to three samples per scanning strategy which were produced with a low, medium and high VED. In this study, we specifically focused on investigating the effects of scan strategies with 0°, 45°, and 90° degree rotations in order to elucidate the influence of anisotropy, heterogeneity, and to facilitate direct examination of the melt pools. While the potential benefits of state-of-the-art scan rotation, (i.e. 67° degrees) is acknowledged, the objective was to provide a comprehensive analysis of the selected rotation angles to establish a solid foundation for understanding the inherent characteristics of the examined microstructures and their associated mechanical properties.

2.4. Density, Microstructural Characterization and Microhardness

The density (ρ) and relative density (ρ_r) of all samples were measured using the Archimedes principle as described in ASTM B962–13, using Eq. (2) and Eq. (3). A scale with a resolution of 0.1 mg was used to weigh the samples in the air (W_{air}) and immersed in isopropanol (W_{iso}). Each sample was dried and re-measured three times. All testing was conducted at room temperature ($20 \pm 2\,°C$) and relative humidity of
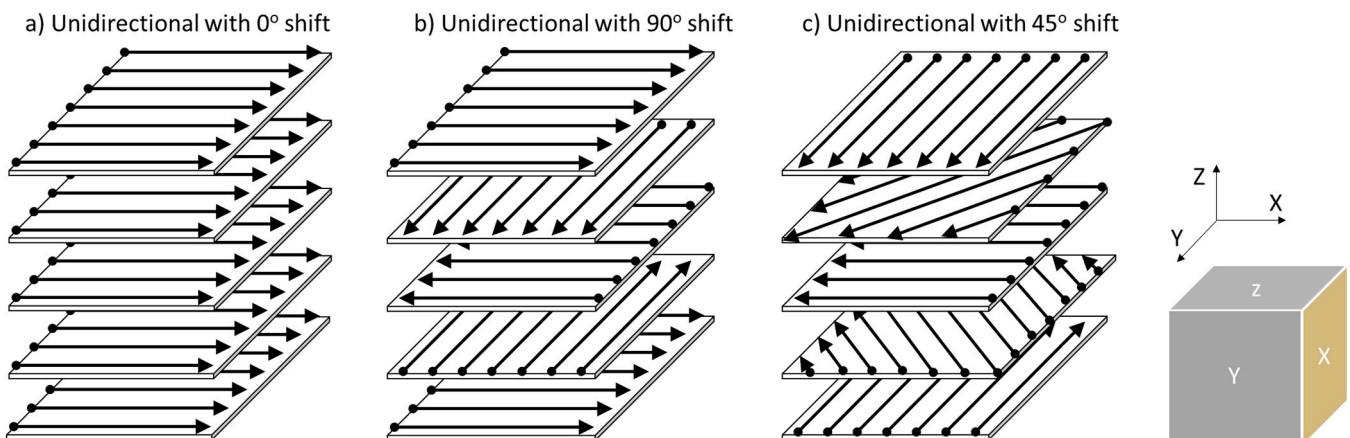

Fig. 2. Examined scanning strategies with building direction along the Z axis.

30–40%. The isopropanol density and the SS316L bulk density were taken as 0.7854 g/cm^3 and 7.99 g/cm^3, respectively.

$$\rho = (\rho_{iso} - \rho_{air}) \times \frac{W_{air}}{W_{air} - W_{iso}} + \rho_{air} \quad (2)$$

$$\rho_r = \frac{\rho}{7.99} \times 100 \quad (3)$$

Microstructural characterization of the sample surfaces was conducted using a TESCAN VEGA scanning electron microscope (SEM) following standard metallographic preparation which included grinding, polishing and a final step of electropolishing. To reveal the finer microstructure, the samples were then etched in aqua regia (3-part HCl to 1-part HNO$_3$).

Microhardness measurements were carried out on all samples that were produced with a 50 μm layer thickness, using a Clark CM Series micro-intender with a diamond Vickers tip by applying a load of 1 kg for 15 s. Vickers hardness values were calculated for each sample by averaging an array of 9 indentations. Particular care was taken to avoid indenting near porosities to minimize the macroscopic effects of porosity. The intention was to obtain hardness values that are affected only by the underlying material microstructure, however, it is recognized that effects from subsurface porosity (or nearby porosity) that is not visible during indentation cannot be avoided.

Additional microstructural characterization was carried out on selected samples from the DOE and the corresponding samples from the scan strategy variation study using a JEOL JSM-7200 F field emission SEM, equipped with an Oxford Instruments C-NANO EBSD detector. Following electropolishing, Kikuchi patterns were collected from the X side of each sample, which corresponds to the surface parallel to the build direction (Fig. 2). The EBSD inverse pole figure (IPF) maps were generated with the AztecCrystal software, using a step size of 2 μm which corresponded to a 1000 × 500 μm^2 field of view. Grain sizes were measured using the area-weighted average grain size metric (Tables 2 and 3).

3. Results and discussion

3.1. Effect of LPBF parameters on densification

Fig. 3 shows the effect of VED on the densification of LPBF 316 L samples, relative to the density of the cast 316 L. Despite the increasing evidence that the current formulation of VED is not sufficient to effectively capture the complex physical phenomena that occur at the melt pool, the metric is widely used as a starting point for optimizing the LPBF parameters. In this work, relative densities over 95% were achieved at VEDs of at least 100 J/mm^3. Above this threshold, the energy transferred to the powder bed sufficiently melts the material, which fills the gaps between successive scans and minimizes the formation of lack-of-fusion porosity. Interestingly though, and contrary to a few literature works [15,16], even at the higher end of VEDs examined (i.e. > 250 J/mm^3), no decrease in the relative density, as a result of excessive melting and evaporation of species, was observed (Fig. 3). The data were fitted with a trendline that intercepts the y-axis at a relative density of 52% (representing the packing density of the powder used) and which asymptotically approaches the 100% relative density. The equation of the trendline is shown in the labels of Fig. 3.

To assess the validity of this trendline and to examine whether the parameters used should, as expected by the literature and theory, produce keyhole porosity, the empirical method proposed by Hann et al.

Table 3
Full factorial Design of Experiments study factors and levels.

Factors	Laser power, P [W]	Scan speed, v [mm/s]	Hatch spacing, h [μm]	Layer thickness, l [μm]
Levels	120	300	42.5	50
	150	600	52.5	75
	180	900	62.5	100
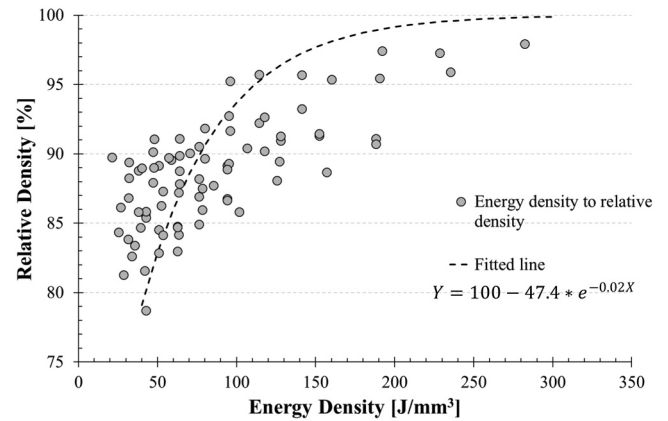
Fig. 3. Relative density against volumetric energy density for the LPBF 316 L samples.

[24], was employed. In the field of laser welding, a shift from the stable conduction mode to the so-called keyhole mode takes place when the energy imposed on the material is sufficient to cause evaporation of the metal. The recoil momentum pressures developed by the metal vapour, exert forces on the molten material resulting in the formation of cavities during solidification [25]. Based on experimental observations of melt pools, Hann et al. proposed the normalized enthalpy rule, which can be used to determine whether a transition to keyhole mode should occur (Eq. 4).

$$\frac{\Delta H}{h_s} = \frac{AP}{\rho h_s \sqrt{\pi D \nu \left(\frac{\sigma}{4}\right)^3}} \quad (4)$$

Where A is the material absorptivity, ν is the scan speed, D is the thermal diffusivity, ρ is the bulk material density and h_s is the enthalpy of the solid material at the melting point. Calculation of the normalized enthalpy was based on a laser power (P) of 180 W, spot size (σ) of 40 μm and scan speed (v) of 300 mm/s, which correspond to the parameters of the highest VED and highest relative density sample. The remaining term values were taken from the available literature at the melting point (T_m) of SS316L and are given in Table 4. Using Eq. 4, the normalized enthalpy value for the highest density sample was calculated at ~159 × 10^3. The threshold normalized enthalpy value for transitioning to keyhole mode was determined for 316 L by King et al. to be 30 [24]. By producing a series of 316 L single-track beads, King et al. measured the melt pool depth and examined whether keyhole mode was achieved. They then used the LPBF process parameters to calculate the normalized enthalpy to determine the transition from conduction to keyhole mode. Assuming the parameters obtained from the literature and the empirical threshold criterion for the keyhole mode used are correct, the question then arises as to why the keyhole porosity and subsequently a drop in relative density, were not observed in this study.

Table 2
Chemical Composition of 316 L powder in wt%.

C	Cr	Cu	Mn	Mo	N	Ni	Si	Traces	Fe
< 0.03	16–18	< 0.75	< 2	2–3	< 0.2	10–14	< 0.75	< 0.1	Balance

Table 4

Physical properties of 316 L taken at T_m= 1673 K.

Property	Value for 316 L	Calculation	Reference
Thermal diffusivity (D)	5 m^2/s	NA	[30]
Absorptivity (A)	5.81×10^{-6}	$A(T) = A_O + 7.1 \times 10^{-5}T$ $A_O = 0.68$ (Absorptivity at RT)	[31]
Enthalpy (h_s)	1.2×10^{-6} J/kg	NA	[25]

The normalized enthalpy criterion was developed based on observations of 316 L single tracks and constitutes an empirical method for determining the transition to keyhole mode. Differences in the LPBF process parameters between this work and the study of King et al. might therefore explain the discrepancy, at least to a certain extent. Firstly, the powder particle size distribution used in their study had a range between 14 and 49.2 μm, which is significantly lower than the one used in this study. This is expected to change the rate of energy absorption and heat dissipation within the powder bed, resulting in different melt pool and microstructure morphologies and ultimately shifting the transition to keyhole mode. Samples produced with smaller powder particles will reach peak densities and consequently keyhole mode at much lower energy densities [26]. In addition, the effect of particle size distribution needs to be evaluated in combination with the layer thickness employed. Spierings et al. [27], experimented with different layer thicknesses and particle size distributions and found that there is an optimal ratio between the effective layer thickness and the 90% median diameter (D90) of the powder particles. It is therefore expected that any significant deviations from the optimal ratio would further exacerbate the differences in the solidification behavior observed between this study and others.

Furthermore, there is a significant difference between heat accumulation and dissipation between single-track experiments, such as those performed by King et al., and the multi-track samples produced for this study. The presence of solid material around the melting pool in a multi-track scan provides additional heat accumulation paths, effectively increasing the thermal energy provided to the material compared to single-track experiments [28]. Even between multitrack samples, changing the scanning direction and sequence has been shown to reduce the accumulated heat and the temperature gradient of the surrounding powder, which in turn alters melting and densification [29].

A combination of the above is expected to have influenced the solidification behaviour of the 316 L samples produced here and has resulted in some differences from the behaviour observed for the same material elsewhere in the literature. The effects of particle size distribution and layer thickness as well as of the scan strategy on the densification of 316 L samples are discussed in more detail in the following sections.

3.2. Design of Experiments study

The effect of each of the major LPBF process parameters (*Laser Power, Scan Speed, Hatch Spacing, Layer Thickness*) as well as their interaction effects on the density of the samples produced was assessed through a full factorial DOE. Initially, the model was run with all interaction parameters (including three and four-way interactions) using a stepwise backward elimination of terms. Using a confidence level of 95% it was found that the three-way interactions had an insignificant effect on the density of the samples. Therefore, to reduce complexity, the regression model was re-run including the effects of up to two-way interactions. The null hypotheses of the model assumed no significant effect between the process parameters or their two-way interactions and the response (i. e. the relative density). The null hypothesis was rejected when the confidence interval was less than 95% (corresponding to a p-value of > 0.05). The regression model was considered statistically significant when the F-value of the accepted terms is greater than the critical value. Table 5 shows the output of the regression analysis, highlighting the parameters that are found to be statistically significant in terms of their effect on the density of 316 L. Eq. 5 represents the regression model derived from the analysis, including only the statistically significant parameters and interactions.

The results indicate that for the range of values examined, hatch spacing does not affect the relative density obtained. In contrast, the other parameters of the VED equation (i.e. laser power, scan speed and layer thickness) significantly affect the resulting density as their value changes (Fig. 4a). Further to the so-called main effects, the regression analysis indicated that the interaction effect of *Laser Power and Scan Speed* with *Layer Thickness* is statistically significant. These significant interaction effects indicate that the relationship between *Laser Power* and *Scan Speed* with relative density depends on the value of the *Layer Thickness*. For example, for a power of 120 W, the highest density is achieved at a layer thickness of 75 μm. However, the highest density for power of 180 W is achieved at a layer thickness of 50 μm. Similar observations can be made for the case of scan speed. All interaction effects are shown graphically in Fig. 4b with the statistically significant ones illustrated with a white background.

$$Relative\ Denisty = 83.65 + 0.1524\boldsymbol{P} - 0.021484\boldsymbol{v} - 0.0000992\boldsymbol{Pl} + 0.000144\boldsymbol{vl}$$

(5)

$\boldsymbol{P}$: Power [W], $\boldsymbol{v}$: Scan Speed [mm/s] and $\boldsymbol{l}$: Layer Thickness [μm].

Table 5

Regression analysis for the relative density of 316 L as a function of the LPBF processing parameters.

Term	DF	Sum of Squares	Contribution	F-Value	P-Value
Constant	10	1096,08	87,09%	47,24	0000
Power	1	296,19	23,53%	9,40	**0003**
Scan Speed	1	595,61	47,33%	7,01	**0010**
Hatch Space	1	0,19	0,01%	0,01	0918
Layer Thickness	1	136,34	10,83%	2,95	**0090**
Power x Scan Speed	1	0,43	0,03%	0,18	0669
Power x Hatch Space	1	0,72	0,06%	0,31	0578
Power x Layer Thickness	1	11,49	0,91%	4,95	**0029**
Scan Speed x Hatch Space	1	1,10	0,09%	0,47	0493
Scan Speed x Layer Thickness	1	47,46	3,77%	20,45	**0000**
Hatch Space x Layer Thickness	1	6,55	0,52%	2,82	0097
Error	70	162,43	12,91%	2320	
Total	80	1258,51	100,00%		
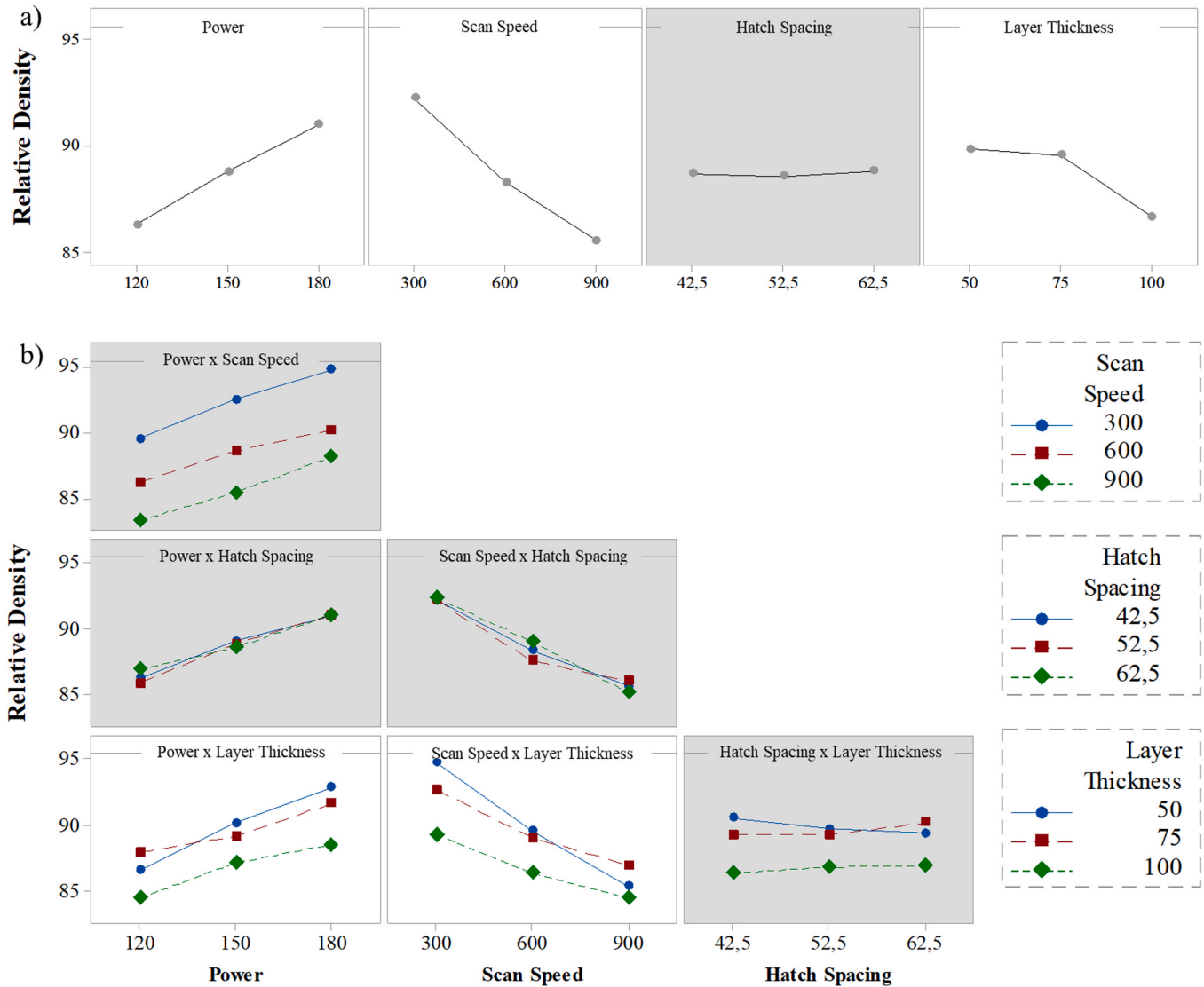
A gray background represents a term not in the model.

Fig. 4. Regression analysis results showing a) the main parameter effects (Power [W], Scan Speed [mm/s], Hatch Spacing [µm], Layer Thickness [µm]) and b) the effects of parameter interactions on the relative density.
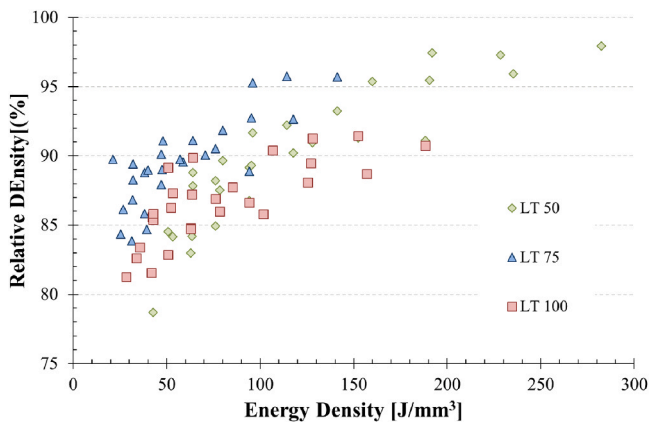

Fig. 5. Relative density against volumetric energy density for the LPBF 316 L samples with respect to the layer thickness.

3.3. Effects of layer thickness and powder size distribution on Densification

As described elsewhere, only part of the volumetric energy density is absorbed by the powder bed material [32]. Other than the intrinsic material properties, the size distribution of the powder particles and consequently their packing density, was shown to have a strong effect on the deposition and absorption of the laser energy [33]. Given the DOE results that showed that the layer thickness should be considered in combination with the other processing parameters, the data in the plot of Fig. 3 were divided in terms of the layer thickness used and replotted as shown in Fig. 5. Upon close observation, it becomes evident that the attainment of peak relative density of 100% varies across the different layer thicknesses: for layer thicknesses of 50 µm and 75 µm, the data indicate a trend towards achieving this density at lower energy density inputs. This trend not only agrees with the findings of the DOE study but also highlights the importance of harmonizing powder size distribution with layer thickness. These findings highlight the potential efficiency of utilizing a 75 µm layer thickness with reduced energy input to achieve optimal productivity, in accordance with the characteristics of the

powder employed in this study.

3.4. Effects of scan strategy on densification

In order to investigate whether the lack of keyhole porosity and a corresponding drop in relative density, is a factor of the scan strategy, selected samples from the 50 μm layer thickness batch were reproduced with the 45° and 90° shift scan strategies. For the selection of the representative samples, the plot of Fig. 3 was divided into three VED regimes. A low (0–80 J/mm^3) where lack of fusion porosity is typically observed, an intermediate (80–180 J/mm^3) which corresponds to the previously reported optimal processing window for 316 L [15,16] and a high (>180 J/mm^3) where keyhole porosity is typically observed. As shown in Fig. 6, the strategies that included rotation of scanning pattern between successive layers, resulted in higher relative densities, particularly at the intermediate section of the graph. At the higher VED regime, data appear to converge as the increasing energy input suppresses any lack of fusion porosity irrespective of the laser path. In agreement with similar observations in the literature [34], rotation between layers increases the overlap between newly and pre-deposited tracks, helping to eliminate lack-of-fusion pores that form at the interface of neighbouring melt pools. However, even though the same track deposition occurs more frequently in the 90° degree rotation samples (i. e. every 2 layers) compared to the 45° rotation samples (i.e. every 4 layers), there are no noticeable differences in their resulting densities across the examined VED range.

3.5. Microstructural characterization

Optimal LPBF conditions are characterized by stable printing (i.e. minimal spattering and balling) which results in homogeneous melt pools with near symmetrical aspect ratios [35,36]. Optical microscopy images of the X side (Fig. 2) of etched samples, from the three scan strategies examined, are shown at various VED builds in Fig. 7. The etched surfaces reveal the characteristic fish scale microstructure associated with the melt lines and the variations in the local chemistry that occurs during solidification at the boundaries of the weld bead. The arrangement of the melt pool pattern reflected the scan strategy employed. Starting at the bottom of Fig. 7 (corresponding to low VED values), a large lack of fusion pore is observed within the entire field of view. As VED increases, lack-of-fusion porosity reduces and is confined in between successive layers or adjacent melt pools. Overall, with increasing VED it was observed that the melt pool size also increases resulting in dense microstructures with several large columnar grains that span across multiple melt pools.
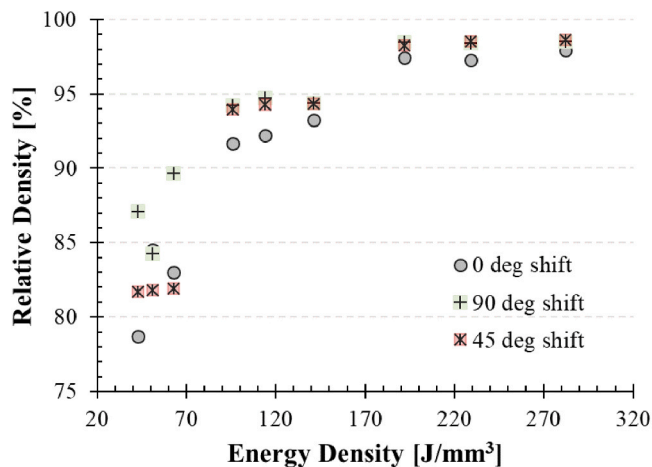

Fig. 6. Relative density against volumetric energy density plots for three scan strategies.

Evidence of keyhole mode can be seen in the melt pool morphology of the highest VED sample with 90 degrees rotation. Even though keyhole porosity is observed to form under these conditions it appears that it did not affect the resulting density significantly. Interestingly, keyhole-shaped melt pools were only observed for the 90° rotation strategy, although the same VED was used with no rotation and 45° rotation scan strategies. It appears that the frequency of rescanning the same track and the heat flux generated with the 90° rotation creates the necessary conditions for keyhole formation, which is then suppressed as the frequency of rescanning increases (i.e. with the 45° rotation).

As shown in Fig. 8 and the EBSD maps of Fig. 9, as the applied VED increases, grains become larger and more elongated along the build direction, irrespective of the scan strategy. However, there are notable differences between the resulting grains in terms of size, morphology and crystallographic orientation. The largest average grain size is obtained for the 0° scan strategy at 282 J/mm^3, followed by the 90° strategy. Compared to the 45° strategy, longer and more columnar grains were developed for the 0° and 90° scan strategies. The decrease of the average grain size with decreasing energy density is attributed to the breakup of the epitaxial columnar growth due to lack-of-fusion porosity that develops in the microstructure.

Decreasing the angle of rotation, or in other words, increasing the number of layers between overlapping laser tracks (overlapping occurs every: 1 layer for 0°, every 2 layers for 90° and every 4 layers for 45°) suppresses the elongation and preferential orientation of grains. Grains in the 45° scan strategy create a less orientated crystallographic texture which appears to favour growth along the < 001 > direction as the frequency of overlapping scan lines is increased. Therefore, to decrease texture and anisotropy finer angles of rotation should be preferred. Similar observations were made by Dovgyy et. al. who observed that more complex scan strategies promote stronger in and out of layer side branching of grains, which resulted in a significant grain broadening and reduction in the degree of verticality [34]. On the contrary, considering the unidirectional strategy with no shifting between layers, energy is regularly deposited in the same tracks, re-melting multiple layers over the same spot and creating large thermal gradients as the samples are built from the bottom to the top. These conditions favor the out of plane (parallel to the build direction) epitaxial growth which results to the most anisotropic microstructure characterized by elongated thin grains. By altering the scan strategy, the angle between consecutive layers and hence the melt pool orientation changes with every powder deposition. Since each pass of the laser penetrates and re-melts previously deposited layers, the flow of metal and the heat flux generated is affected by the scan direction. It is therefore expected that the angle of rotation between successive layers will have a significant effect on the epitaxial growth of grains in LPBF, as it defines the orientation of the new heat flux with respect to the existing [29,34].

3.6. Microhardness

In polycrystalline materials, grain morphology is the key driver of the resulting mechanical properties. Following the investigation of the formation mechanisms associated with the crystallographic texture and grain morphology, the Vickers hardness of the materials, as a representative of their mechanical response, was evaluated. To assess potential plastic anisotropy, each sample was indented on all three orthogonal sides with the same grid pattern. Hardness measurements were taken on samples produced with all three scanning strategies (Fig. 2). To illustrate the effects of scan strategy and anisotropy, the results are plotted in terms of the indentation plane (Fig. 10) and terms of the scanning strategy employed (Fig. 11). The error bars represent one standard deviation in each direction.

Across all measured samples, microhardness was found to increase with energy density, before reaching an apparent plateau at VED values higher than 96 J/mm^3. It should be noted here, that to increase the reliability of the data and minimize the effects of subsurface porosity,
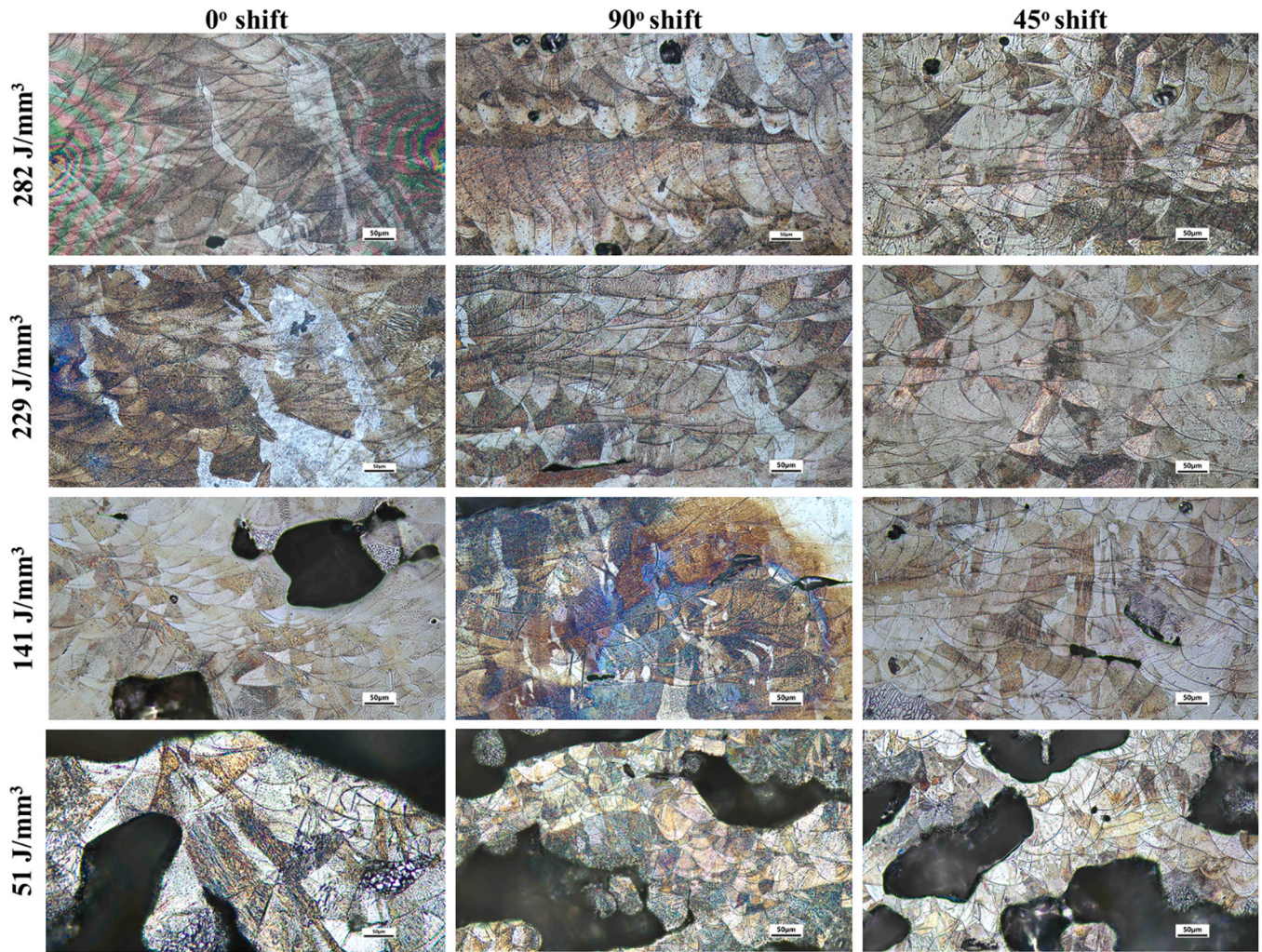
Fig. 7. LPBF melt pool evolution of 316 L with varying volumetric energy density and scan strategies.
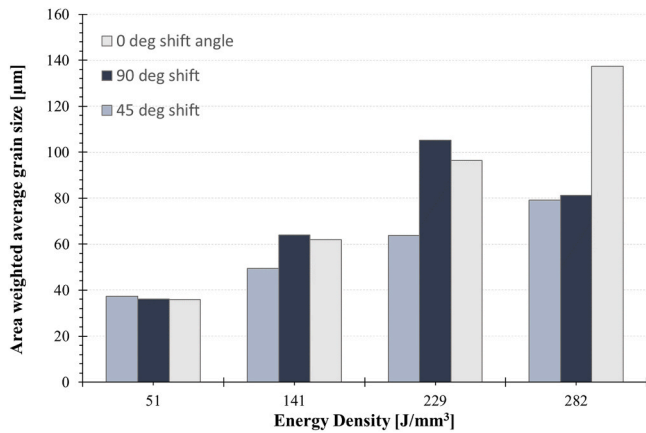

Fig. 8. Area weighted average grain size evolution with increasing energy density and scan strategy variation.

the average hardness values are calculated excluding outliers which were identified using the interquartile rule. This method utilizes the interquartile range to gauge the dispersion of the middle 50% of the data, thereby establishing a range within which data points are considered typical. Any points falling outside this range were disregarded. Despite the exclusion of outliers and the care taken to avoid

porous regions during indentation, it is evident that at low energy densities, porosity has a profound effect on the measured hardness. The effect of porosity is also evident from the large standard deviations obtained for all hardness results associated with low energy density values (i.e. less than 96 J/mm^3).

The maximum average hardness obtained was 233HV, which was measured on the X plane of the 45° shift sample produced with an energy density of 229 J/mm^3. This is consistent with the range of microhardness values reported in the literature [12,23]. Considering only the samples that were produced with higher than 96 J/mm^3 (i.e. samples with low porosity) all hardness values were within 15% of the maximum. Since no particular trends were immediately obvious between the hardness values of the samples examined, a statistical hypothesis T-test with a 95% confidence interval was employed to examine whether the mean hardness values between the two sets are significantly different (i.e. differences observed are not due to random chance). T-test results are shown in the tables of Fig. 10 and Fig. 11 next to the corresponding plot. The significant differences are highlighted at each energy density level for each pair of 0°, 45° and 90° shift rotation. The highlighted cell in the T-test tables indicates the highest value in a pair. An immediate observation was that the majority of statistically significant differences are obtained at the higher range of VEDs. This is mainly due to the effects of porosity and the associated large standard deviations obtained at low VEDs. In general, significant anisotropy was observed between the scan strategies with rotation angles and the unidirectional builds (Fig. 10) as well as between all samples with respect to the Z plane
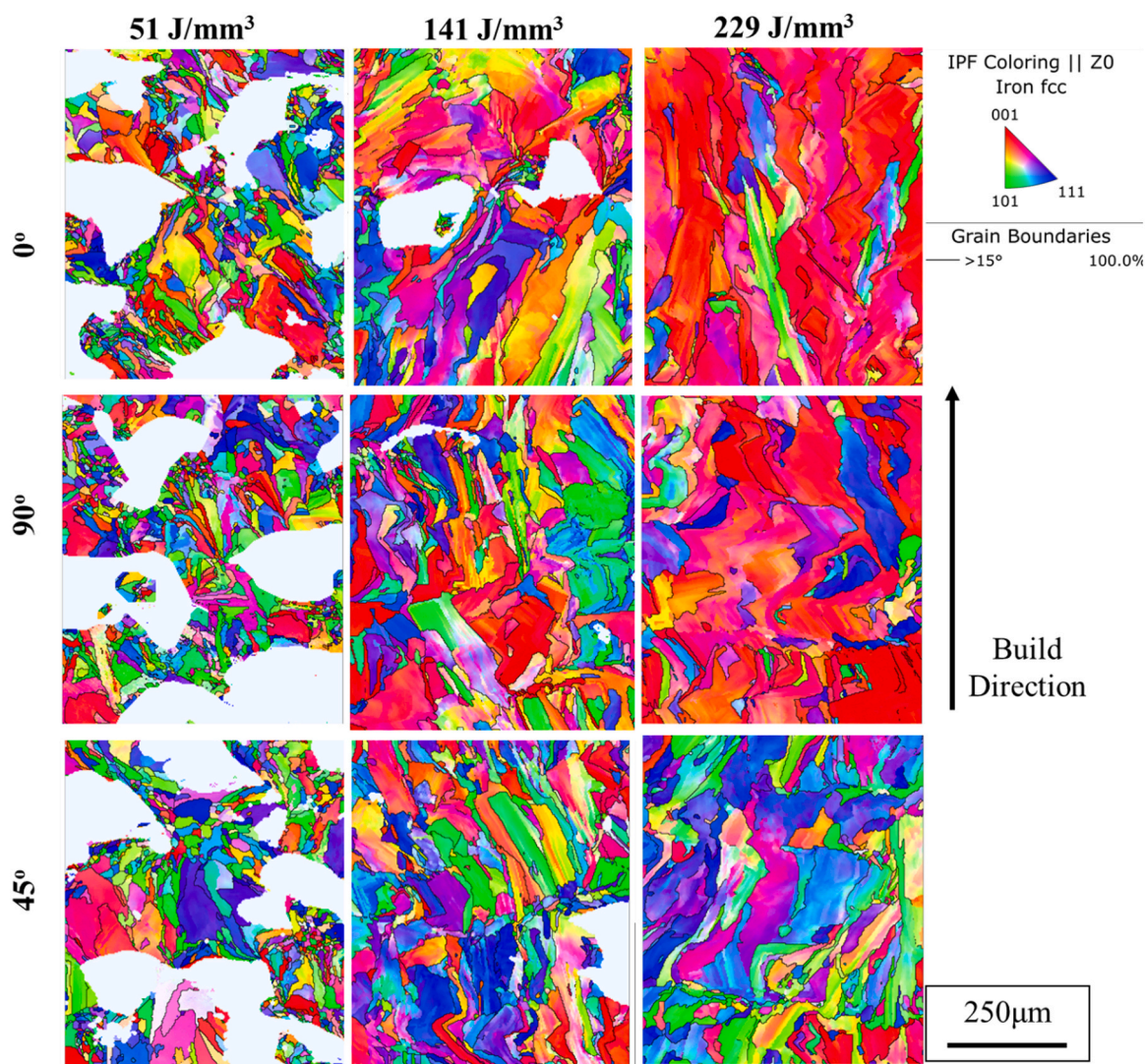
Fig. 9. EBSD maps of the X-side of samples produced with increasing energy density and different scan strategies highlighting the high-angle grain boundaries (>15 degrees).

(Fig. 11). Considering the results obtained on the X plane of the samples (Fig. 10a), a scan strategy with 45° rotation achieves the highest hardness whereas a scan strategy of 90° resulted in the softest X plane. On the contrary, the unidirectional build with no rotation between layers produced the highest hardness Y planes (Fig. 10b), while mixed results were obtained for the Z plane measurements (Fig. 10c).

Contrary to conventional, cast 316 L, the microstructure of LPBF 316 L is characterized by different length scale features, which create a more complex hierarchical microstructure consisting of melt pool layers, grains and sub-grains, cell structures and inclusions [37,38]. As such, several mechanisms can contribute to differences in the mechanical response. Even though samples were produced with the same energy density differences in the resulting microstructure are responsible for the anisotropy observed in hardness measurements. Changes in the laser beam direction for the previously deposited layer alter the heat flux and the direction of the total temperature gradient [39,40], which as seen in Fig. 7 and Fig. 9, alters the resulting microstructure. Therefore, considering the high VED samples where porosity is not expected to affect the resulting microhardness, it is valid to assume that the observed anisotropy is a result of the grain morphology and crystallographic texture. As shown in Fig. 8 and Fig. 9, the grain size and preferential orientation of grain vary depending on the scan strategy employed. It is well known, that deformation in crystalline materials occurs due to

plane slip, according to the Schmid factor of the grains. Favourably oriented grains (i.e. high Schmid factor) deform more easily when stressed as their orientation allows higher resultant forces to act along the preferential slip system of the crystal. In the case of FCC materials, such as the austenitic 316 L, slip is favoured in three directions along the {111} planes. Therefore, it is much harder to activate a slip system when indentations are perpendicular to these planes compared to either the {001} or the {101}. In fact, according to the multiscale modelling work conducted by Li et al., slip is favoured for indentation made on surfaces parallel to the {001}, followed by the {101} and the {111} planes [41]. This is in line with the ranking of the hardness values obtained on the X plane of the samples. The crystallographic texture of the samples produced with 0° and 90° rotation is characterized by elongated {001} grains, whereas the sample produced with a 45° rotation scan strategy has a more random texture with a lot of grains aligned with the {111} planes.

However, hardness differences observed on the equivalent planes of samples produced with different scan strategies cannot be fully explained by crystallographic texture alone. As shown in Fig. 11, hardness values obtained on the Z plane are generally higher. This is particularly profound in the 90° scan strategy (Fig. 11b), where the Z plane exhibits significantly higher hardness compared to both X and Y planes, across most energy densities investigated. In a similar study
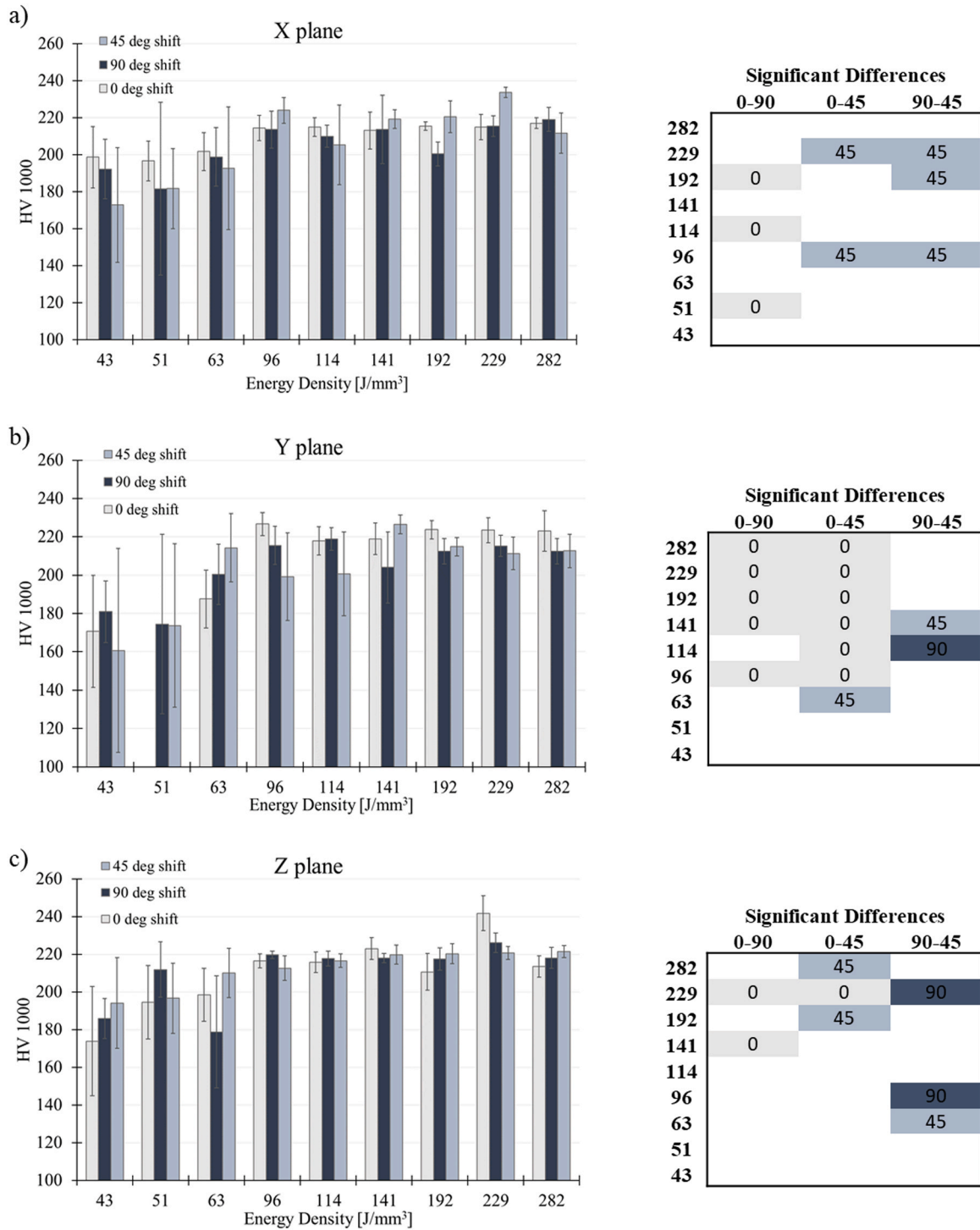
Fig. 10. Comparison of Vickers microhardness values obtained across a range of energy densities on and different scanning strategies for the three orthogonal planes of each sample a) X, b) Y and c) Z. T test results showing significant differences between hardness values resulting from different scanning strategies are shown next to each plot. The highest value is indicated in the corresponding table cell color coded according to the plot data.

conducted by Tucho et. al [23], it was shown that the large columnar grains of the planes normal to the build direction (i.e. X plane here) are projected as smaller and finer grains when viewed from a plane normal to the build direction (i.e. Z plane here). Refined and dislocation-rich microstructures associated with smaller grains, can resist plastic deformation and act as strengthening mechanisms [42]. In view of this, higher Z plane hardness for the 0^0 and 90^0 scan strategies is expected.

According to the well-established Hall-Petch relationship, the strength of crystalline materials (σ) scales inversely proportional to the size of the grain size (D).

$$\sigma \propto D_{av}^{-1/2}$$

During the solidification of the melt pool in LPBF materials, a fine cellular microstructure has been shown to develop within the growing grains. It has been therefore previously argued that the primary cell spacing is the key microstructural feature that controls the mechanical response according to the Hall-Petch relationship. This essentially implies that finer cellular structures in LPBF 316 L have a higher capacity in
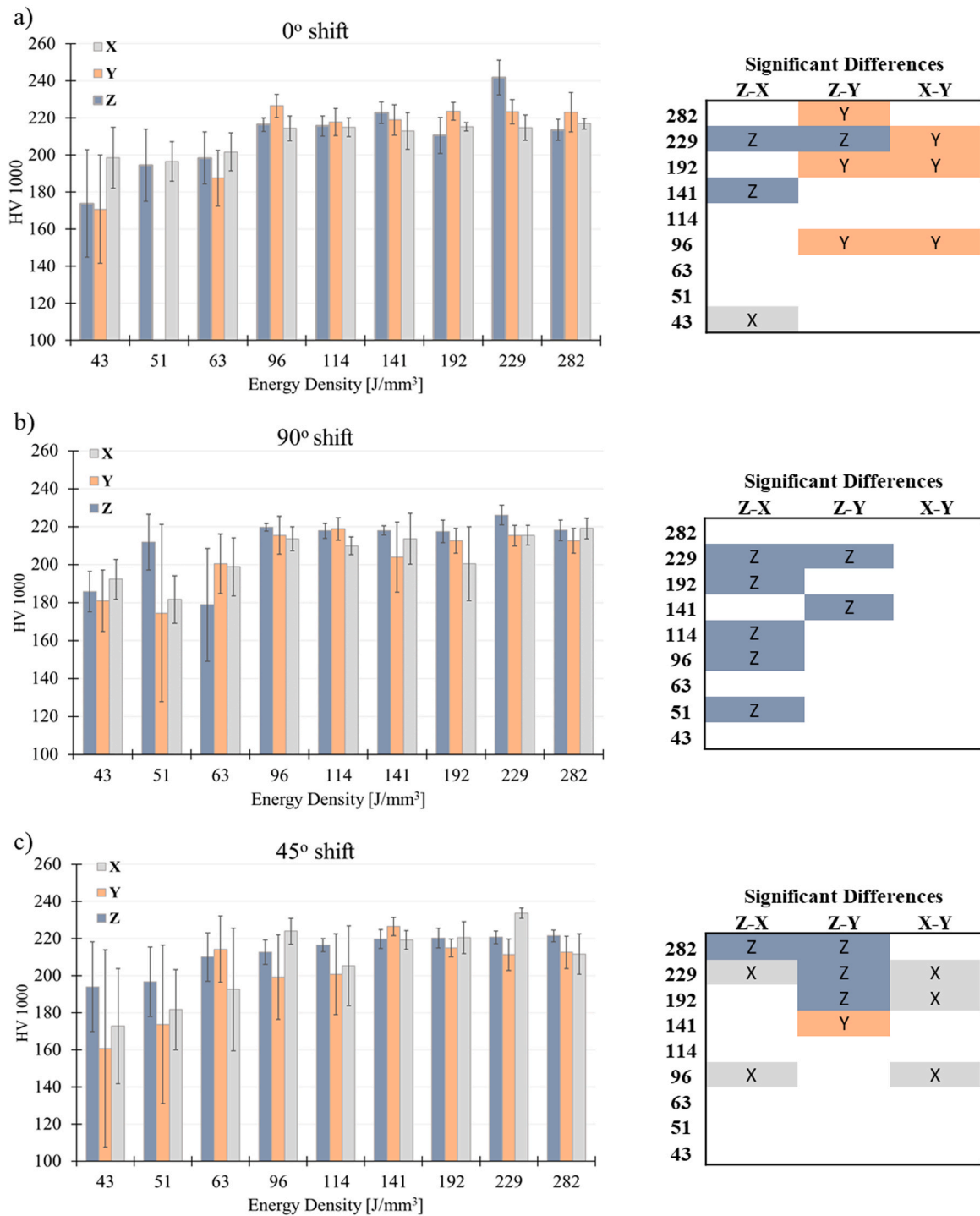
Fig. 11. Comparison of Vickers microhardness values obtained across a range of energy densities on the three orthogonal planes of each sample for different scanning strategies a) 0°, b) 90° and c) 45° rotation between layers. T-test results showing significant differences between hardness values on different planes are shown next to each plot. The highest value is indicated in the corresponding table cell color coded according to the plot data.

resisting plastic deformation during indentation. According to Krakhmalev et al. [18], the primary cell spacing depends on the thermal gradient and solidification rate of the build. The higher the thermal gradient and solidification rates (i.e. higher scan speeds) the smaller the spacing [43]. Unidirectional scan strategies with no rotation are associated with large thermal gradients, which are generally considered unfavourable due to the large thermally-induced stresses generated [44]. However, as discussed, large thermal gradients can lead to refined cellular structures and higher-strength materials. This could explain the behaviour seen in

Fig. 10b, where the Y plane of the 0° scan strategy exhibits the highest hardness. Long, repeating scan lines, stacked on top of each other are expected to generate large thermal gradients and thus smaller cells.

It can be therefore argued that due to the highly complex and hierarchical microstructure of LBPF materials, several strengthening mechanisms can be active simultaneously depending on the loading scenario. Dislocation networks, subgrain structures, crystallographic texture, residual stresses and grain morphology all contribute towards the anisotropy observed in the LPBF 316 L.

4. Conclusions

The comprehensive assessment of 316 L samples produced via LPBF has provided additional insights into the relationship between processing parameters, microstructure and mechanical response. The analysis of a large number of samples through a full factorial design of experiments study that incorporated statistical elements and advanced characterization techniques formulated the conclusions outlined below. It is important to emphasize that the conclusions drawn regarding the influence of VED on defects, microstructure, and hardness pertain specifically to the LPBF system utilized in this study and under the prescribed processing conditions. While these findings contribute to our understanding of the effects of LPBF processing parameters on 316 L stainless steel, it should be acknowledged that different AM machines and alternative parameter settings may yield varying results.

- In addition to the parameters that constitute the VED equation, the quality of consolidation also depends on the scan strategy which is employed, especially at intermediate VEDs (80–120 J/mm^3).
- Matching the process parameters and particularly the powder size distribution with the layer thickness employed can provide higher density values at lower energy density values.
- The empirical normalized enthalpy criterion for defining the keyhole mode did not match the experimental observations of melt pools in this study. The effect of layer thickness, powder size distribution and scan strategy is not fully captured by the normalized enthalpy equation and results can deviate from the prediction.
- Variation of the scan strategy in terms of the rotation angle between successive layers was found to have a significant effect on the crystallographic texture and grain morphology developed as it affects the thermal gradients of the build. Higher cooling rates associated with finer angles of rotation result in smaller equiaxed grains.
- Several competing mechanisms contribute towards the strengthening and plastic anisotropy of LPBF 316 L. Altering the scan strategy and the indentation plane, different hardness values are obtained reflecting the underlying microstructure and the solidification phenomena that took place during LPBF.

Declaration of Competing Interest

The authors declare that they have no known competing financial interests or personal relationships that could have appeared to influence the work reported in this paper.

Acknowledgements

Data declaration

The raw/processed data required to reproduce these findings cannot be shared at this time as the data also forms part of an ongoing study.

References

[1] B. Blakey-Milner, P. Gradl, G. Snedden, M. Brooks, J. Pitot, E. Lopez, M. Leary, F. Berto, A. du Plessis, Metal additive manufacturing in aerospace: a review, Mater. Des. 209 (2021), 110008, https://doi.org/10.1016/J.MATDES.2021.110008.

[2] M. Masoomi, S.M. Thompson, N. Shamsaei, Quality part production via multi-laser additive manufacturing, Manuf. Lett. 13 (2017) 15–20, https://doi.org/10.1016/j.mfglet.2017.05.003.

[3] Z. Sun, X. Tan, S.B. Tor, W.Y. Yeong, Selective laser melting of stainless steel 316L with low porosity and high build rates, Mater. Des. 104 (2016) 197–204, https://doi.org/10.1016/j.matdes.2016.05.035.

[4] S. Sanchez, P. Smith, Z. Xu, G. Gaspard, C.J. Hyde, W.W. Wits, I.A. Ashcroft, H. Chen, A.T. Clare, Powder bed fusion of nickel-based superalloys: a review, Int. J. Mach. Tools Manuf. 165 (2021), https://doi.org/10.1016/j.ijmachtools.2021.103729.

[5] T. Hatakeyama, K. Sawada, M. Suzuki, M. Watanabe, Microstructure development of modified 9Cr-1Mo steel during laser powder bed fusion and heat treatment, Addit. Manuf. 61 (2023), 103350, https://doi.org/10.1016/j.addma.2022.103350.

[6] L. Zhao, L. Song, J.G. Santos Macías, Y. Zhu, M. Huang, A. Simar, Z. Li, Review on the correlation between microstructure and mechanical performance for laser powder bed fusion AlSi10Mg, Addit. Manuf. 56 (2022), 102914, https://doi.org/10.1016/j.addma.2022.102914.

[7] J. Dutta Majumdar, I. Manna, Laser processing of materials, Sadhana 28 (2003) 495–562, https://doi.org/10.1007/BF02706446.

[8] M.A. Balbaa, A. Ghasemi, E. Fereiduni, M.A. Elbestawi, S.D. Jadhav, J.P. Kruth, Role of powder particle size on laser powder bed fusion processability of AlSi10mg alloy, Addit. Manuf. 37 (2021), 101630, https://doi.org/10.1016/j.addma.2020.101630.

[9] I. Yadroitsev, Sel. Laser melting: Direct Manuf. 3D-Objects Sel. Laser melting Met. Powders (2009).

[10] Z. Wang, Z. Xiao, Y. Tse, C. Huang, W. Zhang, Optimization of processing parameters and establishment of a relationship between microstructure and mechanical properties of SLM titanium alloy, Opt. Laser Technol. 112 (2019) 159–167, https://doi.org/10.1016/j.optlastec.2018.11.014.

[11] F. Liu, X. Lin, C. Huang, M. Song, G. Yang, J. Chen, W. Huang, The effect of laser scanning path on microstructures and mechanical properties of laser solid formed nickel-base superalloy Inconel 718, J. Alloy. Compd. 509 (2011) 4505–4509, https://doi.org/10.1016/J.JALLCOM.2010.11.176.

[12] J. Liu, Y. Song, C. Chen, X. Wang, H. Li, C. Zhou, J. Wang, K. Guo, J. Sun, Effect of scanning speed on the microstructure and mechanical behavior of 316L stainless steel fabricated by selective laser melting, Mater. Des. 186 (2020), 108355, https://doi.org/10.1016/J.MATDES.2019.108355.

[13] B. Zhang, L. Dembinski, C. Coddet, The study of the laser parameters and environment variables effect on mechanical properties of high compact parts elaborated by selective laser melting 316L powder, Mater. Sci. Eng. A 584 (2013) 21–31, https://doi.org/10.1016/j.msea.2013.06.055.

[14] C. Kamath, B. El-Dasher, G.F. Gallegos, W.E. King, A. Sisto, Density of additively-manufactured, 316L SS parts using laser powder-bed fusion at powers up to 400 W, Int. J. Adv. Manuf. Technol. 74 (2014) 65–78, https://doi.org/10.1007/s00170-014-5954-9.

[15] Y.Y.C. Choong, K.H.G. Chua, C.H. Wong, Investigation on the integral effects of process parameters on properties of selective laser melted stainless steel parts, Proc. Int. Conf. Prog. Addit. Manuf. 2018-May (2018) 274–279. https://doi.org/10.25341/D4P88S.

[16] M. Yakout, M.A. Elbestawi, S.C. Veldhuis, Density and mechanical properties in selective laser melting of Invar 36 and stainless steel 316L, J. Mater. Process. Technol. 266 (2019) 397–420, https://doi.org/10.1016/J.JMATPROTEC.2018.11.006.

[17] J. Akram, P. Chalavadi, D. Pal, B. Stucker, Understanding grain evolution in additive manufacturing through modeling, Addit. Manuf. 21 (2018) 255–268, https://doi.org/10.1016/J.ADDMA.2018.03.021.

[18] P. Krakhmalev, G. Fredriksson, K. Svensson, I. Yadroitsev, I. Yadroitsava, M. Thuvander, R. Peng, Microstructure, solidification texture, and thermal stability of 316 L stainless steel manufactured by laser powder bed fusion, Met. (Basel) 8 (2018), https://doi.org/10.3390/met8080643.

[19] T. DebRoy, H.L. Wei, J.S. Zuback, T. Mukherjee, J.W. Elmer, J.O. Milewski, A. M. Beese, A. Wilson-Heid, A. De, W. Zhang, Additive manufacturing of metallic components – process, structure and properties, Prog. Mater. Sci. 92 (2018) 112–224, https://doi.org/10.1016/J.PMATSCI.2017.10.001.

[20] K. Kunze, T. Etter, J. Grässlin, V. Shklover, Texture, anisotropy in microstructure and mechanical properties of IN738LC alloy processed by selective laser melting (SLM), Mater. Sci. Eng. A 620 (2015) 213–222, https://doi.org/10.1016/J.MSEA.2014.10.003.

[21] E. Liverani, S. Toschi, L. Ceschini, A. Fortunato, Effect of selective laser melting (SLM) process parameters on microstructure and mechanical properties of 316L austenitic stainless steel, J. Mater. Process. Technol. 249 (2017) 255–263, https://doi.org/10.1016/J.JMATPROTEC.2017.05.042.

[22] T. Larimian, M. Kannan, D. Grzesiak, B. AlMangour, T. Borkar, Effect of energy density and scanning strategy on densification, microstructure and mechanical properties of 316L stainless steel processed via selective laser melting, Mater. Sci. Eng. A 770 (2020), 138455, https://doi.org/10.1016/J.MSEA.2019.138455.

[23] W.M. Tucho, V.H. Lysne, H. Austbø, A. Sjolyst-Kverneland, V. Hansen, Investigation of effects of process parameters on microstructure and hardness of SLM manufactured SS316L, J. Alloy. Compd. 740 (2018) 910–925, https://doi.org/10.1016/J.JALLCOM.2018.01.098.

[24] W.E. King, H.D. Barth, V.M. Castillo, G.F. Gallegos, J.W. Gibbs, D.E. Hahn, C. Kamath, A.M. Rubenchik, Observation of keyhole-mode laser melting in laser powder-bed fusion additive manufacturing, J. Mater. Process. Technol. 214 (2014) 2915–2925, https://doi.org/10.1016/J.JMATPROTEC.2014.06.005.

[25] R. Rai, J.W. Elmer, T.A. Palmer, T. Debroy, Heat transfer and fluid flow during keyhole mode laser welding of tantalum, Ti-6Al-4V, 304L stainless steel and vanadium, J. Phys. D. Appl. Phys. 40 (2007) 5753–5766, https://doi.org/10.1088/0022-3727/40/18/037.

[26] A.B. Spierings, N. Herres, G. Levy, Influence of the particle size distribution on surface quality and mechanical properties in AM steel parts, Rapid Prototyp. J. 17 (2011) 195–202, https://doi.org/10.1108/13552541111124770/FULL/PDF.

[27] A.B. Spierings, G. Levy, Comparison of density of stainless steel 316L parts produced with selective laser melting using different powder grades, Int. Solid Free. Fabr. Symp. (2009). ⟨https://repositories.lib.utexas.edu/handle/2152/88172⟩ (accessed August 8, 2022).

[28] D. Wang, Y. Yang, X. Su, Y. Chen, Study on energy input and its influences on single-track,multi-track, and multi-layer in SLM, 2011 589, Int. J. Adv. Manuf. Technol. 58 (2011) 1189–1199, https://doi.org/10.1007/S00170-011-3443-Y.

[29] H. Jia, H. Sun, H. Wang, Y. Wu, H. Wang, Scanning strategy in selective laser melting (SLM): a review, 2021 1139, Int. J. Adv. Manuf. Technol. 113 (2021) 2413–2435, https://doi.org/10.1007/S00170-021-06810-3.

[30] A.M. Rubenchik, W.E. King, S.S. Wu, Scaling laws for the additive manufacturing, J. Mater. Process. Technol. 257 (2018) 234–243, https://doi.org/10.1016/J.JMATPROTEC.2018.02.034.

[31] C.D. Boley, A.M. Rubenchik, S.C. Mitchell, S.S.Q. Wu, Metal powder absorptivity: modeling and experiment, Pp. 6496-6500. 55, Appl. Opt. Vol. 55 (Issue 23) (2016) 6496–6500, https://doi.org/10.1364/AO.55.006496.

[32] U. Scipioni Bertoli, A.J. Wolfer, M.J. Matthews, J.P.R. Delplanque, J.M. Schoenung, On the limitations of volumetric energy density as a design parameter for selective laser melting, Mater. Des. 113 (2017) 331–340, https://doi.org/10.1016/J.MATDES.2016.10.037.

[33] H.C. Tran, Y.L. Lo, Heat transfer simulations of selective laser melting process based on volumetric heat source with powder size consideration, J. Mater. Process. Technol. 255 (2018) 411–425, https://doi.org/10.1016/J.JMATPROTEC.2017.12.024.

[34] B. Dovgyy, A. Piglione, P.A. Hooper, M.S. Pham, Comprehensive assessment of the printability of CoNiCrFeMn in Laser Powder Bed Fusion, Mater. Des. 194 (2020), 108845, https://doi.org/10.1016/J.MATDES.2020.108845.

[35] I. Yadroitsev, A. Gusarov, I. Yadroitsava, I. Smurov, Single track formation in selective laser melting of metal powders, J. Mater. Process. Technol. 210 (2010) 1624–1631, https://doi.org/10.1016/J.JMATPROTEC.2010.05.010.

[36] M. Averyanova, E. Cicala, P. Bertrand, D. Grevey, Experimental design approach to optimize selective laser melting of martensitic 17-4 PH powder: Part i - Single laser tracks and first layer, Rapid Prototyp. J. 18 (2012) 28–37, https://doi.org/10.1108/13552541211193476/FULL/XML.

[37] A.K. Agrawal, G. Meric de Bellefon, D. Thoma, High-throughput experimentation for microstructural design in additively manufactured 316L stainless steel, Mater. Sci. Eng. A. 793 (2020), 139841, https://doi.org/10.1016/J.MSEA.2020.139841.

[38] X. Wang, J.A. Muñiz-Lerma, O. Sánchez-Mata, M. Attarian Shandiz, M. Brochu, Microstructure and mechanical properties of stainless steel 316L vertical struts manufactured by laser powder bed fusion process, Mater. Sci. Eng. A. 736 (2018) 27–40, https://doi.org/10.1016/J.MSEA.2018.08.069.

[39] N. Nadammal, T. Mishurova, T. Fritsch, I. Serrano-Munoz, A. Kromm, C. Haberland, P.D. Portella, G. Bruno, Critical role of scan strategies on the development of microstructure, texture, and residual stresses during laser powder bed fusion additive manufacturing, Addit. Manuf. 38 (2021), 101792, https://doi.org/10.1016/j.addma.2020.101792.

[40] H.Y. Wan, Z.J. Zhou, C.P. Li, G.F. Chen, G.P. Zhang, Effect of scanning strategy on mechanical properties of selective laser melted Inconel 718, Mater. Sci. Eng. A. 753 (2019) 42–48, https://doi.org/10.1016/j.msea.2019.03.007.

[41] J. Li, Y. Ni, H. Wang, J. Mei, Effects of Crystalline Anisotropy and Indenter Size on Nanoindentation by Multiscale Simulation, (n.d.). https://doi.org/10.1007/s11671–009-9500-x.

[42] K. Saeidi, X. Gao, Y. Zhong, Z.J. Shen, Hardened austenite steel with columnar sub-grain structure formed by laser melting, Mater. Sci. Eng. A. 625 (2015) 221–229, https://doi.org/10.1016/J.MSEA.2014.12.018.

[43] A. Liang, K.S. Pey, T. Polcar, A.R. Hamilton, Effects of rescanning parameters on densification and microstructural refinement of 316L stainless steel fabricated by laser powder bed fusion, J. Mater. Process. Technol. 302 (2022), 117493, https://doi.org/10.1016/J.JMATPROTEC.2022.117493.

[44] J. Jhabvala, E. Boillat, T. Antignac, R. Glardon, On the effect of scanning strategies in the selective laser melting process 5 (2010) 99–109, https://doi.org/10.1080/17452751003688368. ⟨Http://Dx.Doi.Org/10.1080/17452751003688368⟩.